Structure and registry of the silica bilayer film on Ru(0001) as viewed by LEED and DFT†

Edmar A. Soares, [ab] Joachim Paier, [c] Leonard Gura, [b] Kristen Burson, [de] Catherine Ryczek, [d] Zechao Yang, [b] Fernando Stavale, [fb] Markus Heyde [b] and Hans-Joachim Freund *[b]

Silica bilayers are stable on various metal substrates, including Ru(0001) that is used for the present study. In a systematic attempt to elucidate the detailed structure of the silica bilayer film and its registry to the metal substrate, we performed a low energy electron diffraction (I/V-LEED) study. The experimental work is accompanied by detailed calculations on the stability, orientation and dynamic properties of the bilayer at room temperature. It was determined, that the film shows a certain structural diversity within the unit cell of the metal substrate, which depends on the oxygen content at the metal-bilayer interface. In connection with the experimental I/V-LEED study, it became apparent, that a high-quality structure determination is only possible if several structural motifs are taken into account by superimposing bilayer structures with varying registry to the oxygen covered substrate. This result is conceptually in line with the recently observed statistical registry in layered 2D-compound materials.

1. Introduction

Silicon dioxide (SiO_2) is one of the most abundant and yet still complex materials on earth. As an important raw material for modern technology, silica has been widely used in micro-electronics and catalysis.[1,2] Its function depends on many parameters, including structure.[3,4] In order to shed light on the connection between function and structure, thin silica films supported on a metal substrate have been prepared. The quality of the created films, naturally, depends on structural parameters at the support interface and the formed oxide.[5,6] Once well-structured systems have been prepared, they may be studied at the atomic level with spectroscopic and structure determining experimental tools, both in ultra-high vacuum (UHV) or under ambient conditions. Such tools include scanning tunnelling microscopy (STM), scattering experiments, vibrational and electronic spectroscopy, diffraction and scanning probe techniques.

The acceptance of the general structure of the film as a silica network followed from a long history.[7–16] In the present paper we are discussing the structure of a bilayer SiO_2 film on Ru(0001) with the schemes as shown in Fig. 1 in top and side view.[15,17,18] The structural models are based on density functional theory (DFT) calculations in combination with STM measurements.[15] Each Si atom resides in the middle of a SiO_4-tetrahedron and the tetrahedra are connected *via* oxygen bridges to form a hexagonal lattice structure. In each tetrahedron within the hexagonal arrangement one O atom is shared between a top and a bottom layer forming a so-called bilayer. This crystal structure has been shown to be consistent with results of a number of experimental techniques, including STM, X-ray photoelectron spectroscopy (XPS) and infrared spectroscopy. The bilayer may also be prepared in a vitreous form, representing amorphous silica, again verified through STM measurements.[19,20] The crystalline silica bilayer is known from calculations to be bound to the substrate by dispersive forces only. This leaves a space of a few Ångström between the substrate and the film, where the distance depends on how much oxygen is adsorbed on the metal substrate. The latter information is up to today only available from theoretical calculations, as an analysis of the 3D structure of the system has, so far, not been reported. Due to the preparation procedure, there is always oxygen adsorbed at the interface. The oxygen concentration at the interface may be changed by heating. In a separate set of studies,[21,22] this arrangement has been used to perform model studies on reactions in the confined space between the silica film, which is used as a membrane, and the metal substrate where an adsorbed reaction partner resides. Specifically water forms by exposing the system to hydrogen,

a Department of Physics, Federal University of Minas Gerais, Brazil

b Fritz-Haber-Institute of the Max-Planck Society, Faradayweg 4-6, 14195 Berlin, Germany. E-mail: freund@fhi-berlin.mpg.de
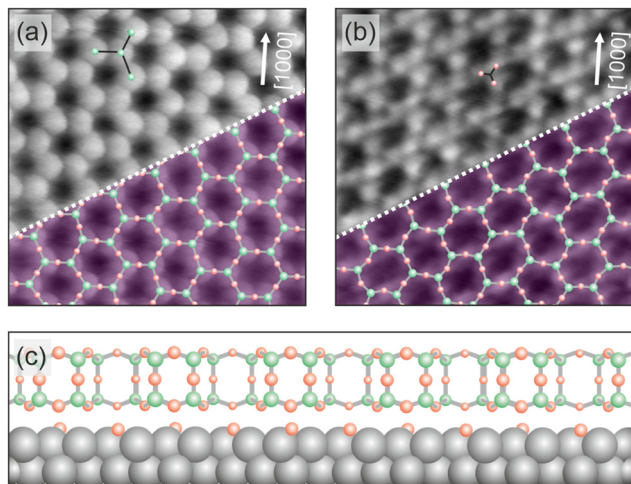
c Institut für Chemie, Humboldt-Universität zu Berlin, 10099 Berlin, Germany

d Hamilton College, Clinton, New York 13323, USA

e Grinnell College, Grinnell, Iowa 50112, USA

f Centro Brasileiro de Pesquisas Físicas, Rio de Janeiro, Brazil

† Electronic supplementary information (ESI) available. See DOI: https://doi.org/10.1039/d2cp04624e

Fig. 1 Structure of the 2D silica film on Ru(0001). Atomically resolved STM images of crystalline silica film regions are given in (a) and (b). The scan area of the two images is 3.5 nm × 3.5 nm. The images have been taken from ref. 23. (a) The imaging contrast reveals the position of Si atoms (V_S = 3.0 V, I_T = 100 pA), while in (b) a contrast towards the arrangement of O atoms is visible (V_S = 100 mV, I_T = 100 pA). White arrows indicate one crystallographic axis of the Ru(0001) substrate. In the lower right corner of (a) and (b) an atomic model of the topmost layer of the silica film is superimposed (green balls: Si atoms, red balls: O atoms). (c) A schematic side view of the silica film structure on the Ru(0001) substrate is plotted.

which diffuses through the six-membered ring of the silica film and reacts with adsorbed oxygen on the metal support, *i.e.* Ru(0001) after dissociation at the surface. On the basis of the analysis of the observed kinetics, with the help of theoretical electronic structure calculations, it was suggested that the bilayer silica film allows for lateral and vertical motions during the reaction as the oxygen concentration at the interface varies while the reaction progresses. This consideration was leading to a consistent description of the observed apparent activation energy. The result triggered the idea to look into more detail of the 3D structure of the silica bilayer film on the metal support, which had not been carried out so far. In order to experimentally determine the structure, and, in particular, the distance between the film and the substrate, as well as its position with respect to the substrate, we here present a first low energy electron diffraction (I/V-LEED) study, together with a set of detailed DFT calculations.

The outcome of the present study reveals atomic level details, which connect not only to the results of the water formation study in confined space, but also to the recently discussed stacking disorder predicted, and observed, for three-dimensional compounds, consisting 2D-layers, where the layers are bound by dispersive forces.[24] So far, often the structure of layered compounds, such as layered zeolites or layered covalent organic frameworks (LCOF), have been assumed to be characterized by fixed stacking of the layers based on X-ray diffraction. However, more recent detailed studies again using x-ray diffraction in combination with theoretical calculations, have revealed stacking disorder.[21,25,26] Also, for graphene on Ni(111) co-existing structures been detected by XPS, where the graphene

film is shifted with low activation energy between two positions on the metal surface.[27] The experimental results, presented in this study, are paralleled and interpreted on the basis of extensive DFT calculations on the possible structural scenarios, as well as the phononic properties of those systems, augmented by molecular modelling calculations. The latter play a decisive role in understanding the details of the structure and revealed unexpected insight.

2. Theory

2.1 Structure optimizations and potential energy scans: computational details

Electronic and ionic structure optimizations have been carried out using the Vienna ab initio simulation package, VASP.[28,29] Projector augmented wave method (PAW[30,31]) pseudopotentials for Ru include the 4s and 4p electrons of the Kr-core in the valence and were generated based on the electronic configuration $4s^2 4p^6 4d^8$ employing the Perdew, Burke, and Ernzerhof (PBE[32]) generalized-gradient approximation for exchange and correlation effects. Oxygen and silicon pseudopotentials use the valence electron configurations $2s^2 2p^4$ and $3s^2 3p^2$, respectively. These potentials correspond to the released version 5.4. A plane wave kinetic energy cut-off of 450 eV and a first order Methfessel–Paxton smearing of 0.1 eV has been used. This ensures minimal fictitious electronic entropy contributions of the order of 10 meV, well below the recommended value of 1 meV per atom. The break criterion for electronic relaxation was set to 10^{-5} eV. Structures were relaxed based on a maximum atomic force criterion of 0.02 eV Å^{-1}. Brillouin zones of (2 × 2) surface unit cells were sampled using a Monkhorst–Pack[33] grid of (6 × 6) k points. These k-point grids were tested, and deviations between total energies obtained using (6 × 6) and (8 × 8) grids are less than 0.01 eV per atom. A vacuum region of 12 Å between top- and bottom-most atoms of repeated slab models has been employed. Scans for the potential energy surfaces (PES) in lateral directions (parallel to the substrate surface) use (6 × 6) cells together with a (2 × 2) k-point sampling. Three Ru layers were used to model the metal substrate.[21] Calculation of the average potential in the surface show that three-layer models suffice to describe the work function accurately (Fig. S1) as shown in the ESI.† PES scans vertical to the substrate surface (Table S1 and Fig. S2–S4, ESI†) use (2 × 2) unit cells with (6 × 6) k points. The distance of the silica bilayer to the metal surface is defined as the distance of the O atoms in SiO_2 bilayer closest to the Ru surface and the average of the vertical positions, *i.e.*, z-coordinates, of the optimized or relaxed Ru surface atoms.

Regarding van der Waals-type dispersion interactions, this work employs Grimme's D2 approach[34,35] to correct energies and gradients. Following previous work, for Ru atoms, the C_6 coefficient of the noble gas Kr has been employed (Table S2, ESI†), *i.e.*, considering core electron contributions only. Employing the C_6 coefficient of a noble gas core, for instance Ne in Mg^{2+} ions, has been recently positively assessed for CO, CO_2, and alkane adsorption on oxide surfaces, metal–organic

frameworks, as well as zeolites.[36] Herein, this ansatz is motivated by supposed complete delocalization of the valence electrons in Ru and will be referred to as DFT+D2′ [37,38] throughout this work. This means that seven 4d and one 5d valence electrons are supposed to be delocalized in metallic Ru. To check the impact of this approach, scans of the silica bilayer vertical to the Ru surface using default C_6 values for Ru, i.e. 24.67 instead of 12.01 J nm^6 mol^{-1}, have been accomplished. Distances of oxygen atoms in SiO$_2$ closest to surface Ru atoms corresponding to energy minima are shown in the first column of Table S1 (ESI†). These distances (PBE+D2) are ca. 5% shorter compared with PBE+D2′ results, and the effect is most pronounced for the clean Ru(0001) surface. For the 3O system, which is probably dominated by electrostatic interactions between SiO$_2$ and the oxygen atoms (or ions) in the surface, varying C_6 in Ru atoms affects the optimal film-metal distance less.

The actual values of van der Waals C_6 coefficients and radii R_0 employed for Ru, Si, and O are summarized in Table S2 (ESI†). The default global scaling factor, $s_6 = 0.75$, being optimal for the PBE functional, has been employed.

Cross sections of the PES have been obtained by shifting or translating the silica bilayer across surfaces along six crystallographic directions as shown in Fig. S6 (ESI†). These cross sections, which are summarized in Fig. S7–S9 (ESI†), correspond to single points based on optimized structures (local minima). The height of the bilayer has been fixed to 3.18, 3.37, and 3.78 Å for the clean Ru(0001), the 1O, and the 3O substrate, respectively. For the clean surface and the 1O system, these values are 0.4 Å larger than those published in ref. 18, but have been chosen in view of the dynamics of the bilayer discussed in the following section. This dynamic behaviour suggests an average distance slightly off the global minimum, and cross sections were computed to represent the effective potential energy landscape "felt" by the bilayer on the surfaces at finite temperatures. Depending on directions, the bilayer has been shifted by two lattice constants. Along this shift, 20 single point structures have been obtained by linear interpolation between initial and final structures (Fig. S7–S9, ESI†). To test for possible relaxation effects, selected single points have been optimized. Based on these tests, relaxation effects are small. The energy lowering was found to be within 0.005–0.010 eV/(2 × 2)cell.

2.2 Molecular dynamics simulations: computational details

To accomplish molecular dynamics (MD) simulations of several tens of ps, machine learned force fields (MLFF) were employed. We use the MLFF implementation within VASP.6.[39,40] These force fields were trained via NVT ensemble DFT-MD simulations employing PBE+D2′ at 300 K using a Nosé–Hoover thermostat.[41,42] The training was done in a stepwise manner. First, a force field for the free silica bilayer has been trained using (2 × 2), (4 × 4), and (6 × 6) unit cells in order to provide an increasing number of atoms. Each training run consisted of 2000 steps of 1 fs. This has been sufficient to ensure Bayesian errors in the total energy/atom and forces to be less than defaulted thresholds. The so-called spilling factor[43] has been three to four orders of magnitude smaller than the default value 0.02. After

the successful training of the force fields for the free bilayer, the above procedure has been repeated for the Ru(0001) supported bilayer using again (2 × 2), (4 × 4), and (6 × 6) unit cells in repeated slab models. This force field had been used as a starting point for 1O and 3O structures. The training of corresponding force fields was again restarted using (2 × 2), (4 × 4), and (6 × 6) unit cells until Bayesian errors have been small enough to ensure accurate forces.

During the actual MD runs based on the abovementioned force fields, desorption of the SiO$_2$ bilayer from the Ru surface occurred occasionally. These desorption events were not observed in simulations based on PBE+D2′, which comprised approximately 9000 steps of 0.5 fs. We explain the desorption when using force fields by the missing dispersion interactions, which are responsible for bonding the film to the metal surface. Because the MLFF is based on a decomposition of the total energy in terms of local contributions, long-ranged dispersion-type of interactions cannot be accurately described by MLFF.[39] Therefore, to prevent desorption of the bilayer during MD runs, a slab model with reduced vacuum height has been used during simulations. We repeated simulations at various distinctly larger vacuum gaps, but the trends or differences in findings reported below were unaffected. Herein reported calculations use a vacuum gap which is slightly larger than twice the equilibrium distance between bilayer and Ru surfaces, i.e., ca. 5–6 Å. For the simulations a (6 × 6) unit cell has been used. The temperature has been set to 300 K and 100 000 steps of 0.5 fs have been carried out. During these simulations of 50 ps, every 100th structure has been printed. In order to estimate atomic amplitudes of the bilayer during simulations, the following equation has been used

$$[u_x](t) = \frac{1}{N_X} \cdot \sum_{i=1}^{N_X} (x_i(t) - x_i^{\mathrm{ref}}), \quad X = \mathrm{Si, O}, \qquad (1)$$

where the time t corresponds to the individual structures (or snapshots) printed during 50 ps simulations.

To define these deviations or amplitudes the reference structure (superscript ref) corresponds to the last or final structure that has been printed. It is supposed that this structure relates to an equilibrated structure. The averaging over index i of length N_X corresponds to the average over Si or O atoms in the bilayer.

The average squared amplitude, $\langle u^2 \rangle$, is defined as

$$\langle u_x^2 \rangle = \frac{1}{M \cdot N_X} \sum_{i,j=1}^{N_X, M} \left(x_{ij} - x_{ij}^{\mathrm{ref}} \right)^2, \qquad (2)$$

where M is the total number of printed structures (usually 1000, see discussion below).

Analogous equations have been used to calculate y and z components of these average squared amplitudes.

3. Structural determination

3.1 Experimental details

The experiments were carried out in an ultra-high vacuum (UHV) chamber system (10^{-10} mbar range) equipped with

STM and I/V-LEED instruments described in ref. 44. The Ru(0001) single crystal was cleaned by repeated cycles of annealing in oxygen atmosphere (2×10^{-6} mbar) for 30 min at 1250 °C, Ar$^+$ bombardment, and annealing in UHV to 1250 °C for 1–2 min. Prior to the silica deposition, the ruthenium surface was covered with oxygen by exposing the clean Ru(0001) surface to molecular oxygen (5×10^{-6} mbar) at 930 °C for 10 min. Subsequently, silicon was evaporated in oxygen atmosphere (5×10^{-7} mbar) for 12 min. After the silicon deposition, the sample was heated to 860–870 °C for 15 min in 5×10^{-6} mbar O_2. Based on previous studies and experiments, this optimal annealing temperature is chosen to minimize the coexistence of vitreous structures.[45–47] When the sample is cooled down to room temperature in the same oxygen pressure, a final annealing step in UHV at lower temperatures of 630 °C was performed to clean the sample surface.

The individual sample preparation procedures have been verified by using STM. Fig. 2 shows STM images of the resulting silica film recorded at room temperature with a beetle-type STM.[44] The silica film exhibits a coverage of 1.8 monolyer (ML) and shows crystalline patches as shown in Fig. 2b. The characteristic ring structure is marked with green hexagons.

After the final annealing step, I/V-LEED curves were recorded at room temperature using the experimental setup as described in ref. 48. Fig. 3 shows the LEED pattern recorded at electron energies of 100 eV. The absence of concentric ring patterns indicates the dominance of crystalline silica patches in the film system. Fig. 3b marks some of the distinct diffraction spots that are used to extract the experimental I/V-LEED curves. The corresponding color legend is shown on the right.

The tracking of the diffraction spot intensities as a function of electron energy was performed using a freely available software package described in ref. 49.

The I/V-LEED quantitative structural analysis was carried out using the method of symmetrized automated tensor LEED[50] with the associated programs to calculate the scattering phase shifts using the approximation of the muffin-tin potential. The muffin-tin potential and the phase shifts were calculated using the Barbieri/Van Hove Phase Shift Package.[50] In particular, a self-consistent Dirac–Fock approach was used to compute the atomic orbitals for each element. The muffin-tin potential was then evaluated following Mattheiss' prescription
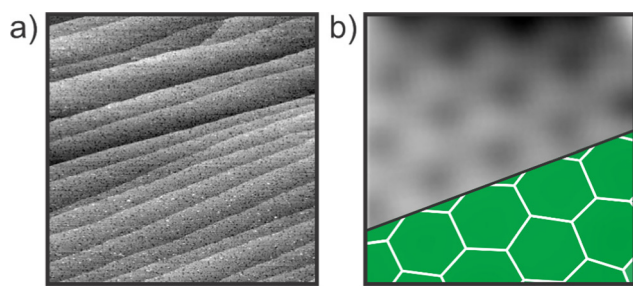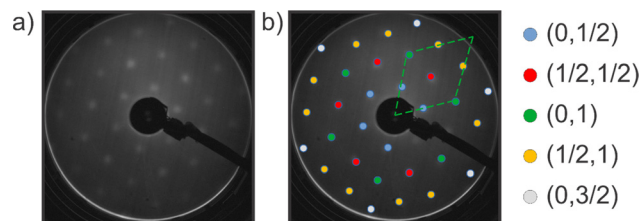
Fig. 3 LEED pattern of the silica bilayer on Ru(0001). (a) Diffraction pattern acquired at 100 eV and (b) with color coded diffraction spots.

- (0,1/2)
- (1/2,1/2)
- (0,1)
- (1/2,1)
- (0,3/2)

and the relativistic phase shifts were calculated by numerical integration of the Dirac equation.

4. Results and discussion

In this section we will first present the results of DFT calculations. They are discussed with respect to the question, which energies are necessary to shift the bilayer silica film parallel to the Ru(0001) substrate. Hereby, comparing the oxygen free interface with two oxygen covered surface configurations, *i.e.* the so-called 1O and the 3O surface. The first one contains one oxygen atom in the unit cell, the second one three oxygen atoms and represents saturation coverage. We then move to a discussion of the MD calculations before we discuss the experimental results of the present I/V-LEED study in light of theoretical results.

4.1 Results and discussion of electronic structure calculations

Fig. 4 shows the PES cross section of the silica film when rigidly translated in [$2\bar{1}\bar{1}0$] direction (or in direction of any of the other rotationally equivalent base vectors, Fig. S6, ESI†). The structure shown in the beginning corresponds to a metastable state at +0.67 eV relative to the minimum energy structures. Vibrational characterization of this and the other metastable structures yield one imaginary mode in translational or shifting direction. It
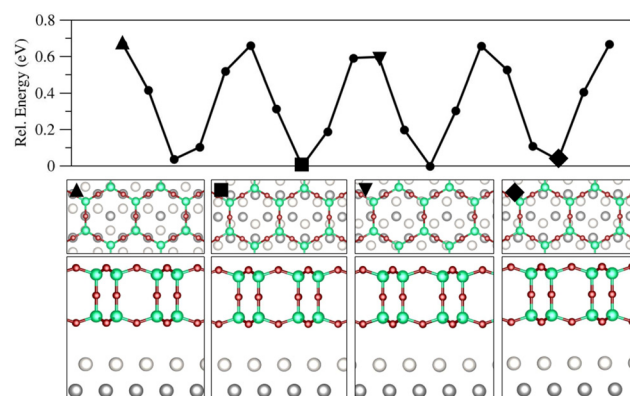
Fig. 2 STM images verifying the preparation of the silica bilayer on Ru(0001). (a) V_S = 4.2 V, I_T = 100 pA, scan area = 500 × 500 nm². (b) V_S = 3 V, I_T = 350 pA, scan area = 2 × 2 nm².

Fig. 4 Cross section of the PES for the bilayer on the clean Ru(0001) surface with an energy barrier of 0.67 eV obtained using PBE+D2′ (upper panel). The bilayer is translated along [$2\bar{1}\bar{1}0$] corresponding to direction 06 in Fig. S7 (ESI†). Below, top and side views for marked single points are shown. Colour code: Ru$_{surf}$ is light grey, Ru$_{sub}$ is dark grey, Si is dark green, and O atoms in the bilayer are dark red.

appears that the responsible structural feature of the bilayer relative to the Ru surface is the position of downward pointing O_3 units of the SiO_4 tetrahedra (triangular face). In high energy or metastable structures the oxygen atoms in O_3 faces are close to or in atop position to Ru_{sub} atoms (triangle in Fig. 4), while Si atoms are close to or in atop position of Ru_{surf} atoms. In contrast, the most stable structures are those with the oxygen atoms in the O_3 face near Ru_{surf} atoms and the Si atoms approximately bridging Ru_{surf} atoms and hcp sites (Ru_{sub}). The above-mentioned energy barrier of 0.67 eV is estimated by taking the difference between highest and lowest energies found for the various structures shifting the (6 × 6) cell of SiO_2 bilayer parallel to Ru(0001) surface in $[2\bar{1}\bar{1}0]$ direction (06 in Fig. S7, ESI†). This is a relatively small barrier which may be overcome at room temperature, indicating that the film may easily be shifted under those conditions.

The energy profiles shown in Fig. 5 and Fig. S8 (ESI†) for the bilayer translated on the 1O surface are substantially different compared to the profiles for the clean surface. Although bilayer heights with respect to Ru_{surf} atoms are comparable (3.18 vs. 3.37 Å), energy barriers for the 1O system are 4.1 eV compared to 0.67 eV for the clean surface. Nonetheless, these cross sections of the PES reflect the symmetry of the surface. Note that the three-fold rotational symmetry of the clean Ru(0001) is preserved in case of the 1O overlayer structure. The scan starts at the low energy "O centred" structure, which means that O_{surf} is centred with respect to the ring of the bilayer (Fig. 5, first triangle). Regarding the Si atoms, one of the two per primitive unit cell is located at a Ru fcc site, and the second one is in an atop position to Ru_{surf}. The downward pointing O_3 units of individual SiO_4 groups are collectively in the atop position to Ru_{sub} atoms. These energy barriers relate to structures where O ions of the bilayer are in atop position of surface O ions. The repulsive electrostatic interaction between these O ions causes the substantial destabilization. Normal mode analysis yields two orthogonal translational modes shifting the bilayer away
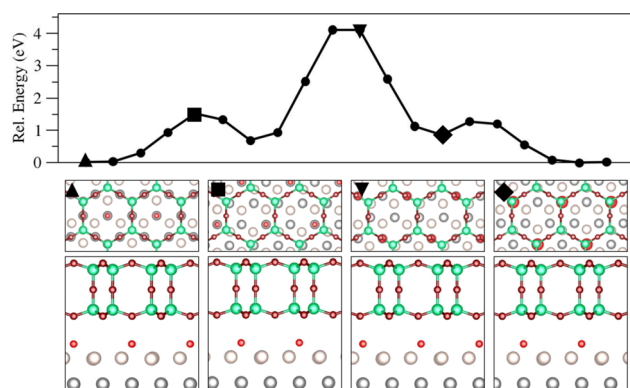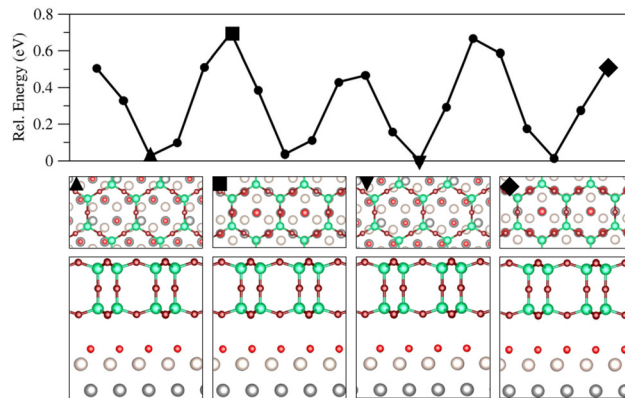

Fig. 6 Cross section of the PES for the bilayer on the 3O-(2 × 2) surface with an energy barrier of 0.70 eV obtained using PBE+D2′ (upper panel). The bilayer is translated along $[\bar{1}2\bar{1}0]$ corresponding to direction 02 in Fig. S9 (ESI†). Below, top and side views for the marked single points are shown. Same colour code as in Fig. 4. For the sake of clarity in top views, radii of interfacial O ions have been notably increased.

from oxygen. Therefore, due to surface symmetry, the energy barrier corresponds to a second order saddle point. These modes are along the short and the long axis connecting interfacial or surface oxygen ions.

Fig. 6 shows an energy profile for the bilayer translated on the 3O surface structure. The direction corresponds to $[\bar{1}2\bar{1}0]$ as displayed in Fig. S6 (ESI†) and features energy barriers of 0.70 eV, which are only slightly higher compared to the clean Ru support. Because of the higher O loading, it appears that some directions feature more and flatter potential wells in contrast to the clean Ru surface and the 1O overlayer structure. Like in previous structures, energy barriers are caused by repulsion of bilayer and interfacial oxygen ions when in atop positions. Conversely, stable structures avoid repulsive interactions among these aforementioned ions by adapting staggered instead of eclipsed configurations (second triangle, Fig. 6). Si atoms of SiO_4 units occur in atop to Ru_{surf} as well as in fcc hollow sites.

4.2 Results and discussion of molecular dynamics

Fig. 7 shows results for amplitudes of the bilayer Si atoms in different directions evaluated according to eqn (1) for three systems: the clean Ru(0001) surface (black lines), 1O (red lines), and 3O (green lines). The amplitudes in z direction for the bilayer on the clean surface indicate an equilibration period within the first 20 ps. The amplitude of the entire bilayer is within a range of ±0.2 to ±0.3 Å. That the entire bilayer wiggles, can be shown by comparing the amplitudes of the bilayer oxygen atoms (Fig. S10, ESI†). These oxygen atoms show the same time evolution. Therefore, one can conclude that the centre of mass of the bilayer is subject to these oscillations normal to the surface. Beyond 20 ps of transient oscillations the amplitude in z-direction decreases and amounts to ±0.15 to ±0.2 Å approximately. Conversely, in x and y directions, parallel to the surface the bilayer drifts at least within 3–4 Å. This drift is not linear. It is akin to an ellipsoid motion.

Fig. 5 Cross section of the PES for the bilayer on the 1O-(2 × 2) surface with an energy barrier of 4.1 eV obtained using PBE+D2′ (upper panel). The bilayer is translated along $[\bar{1}100]$ corresponding to direction 01 in Fig. S8 (ESI†). Below, top and side views for the marked single points are shown. Same colour code as in Fig. 4. Interfacial oxygen ions are light red. For the sake of clarity in top views, radii of these atoms have been notably increased.
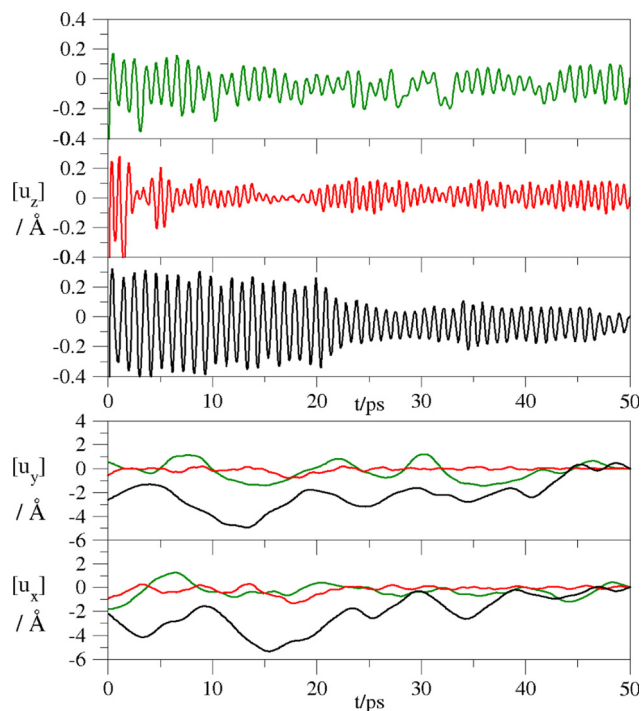
Fig. 7 Deviations or amplitudes (Å) as a function of time t (ps) for Si atoms in the bilayer in x-, y, and z-directions with respect to the final structure obtained using MLFF-MD simulations. These time-evolutions are shown for the clean Ru(0001) (black), 1O (red), and 3O (green) systems. For clarity reasons, the upper three panels show amplitudes in z-direction for each system separately. Lower two panels show analogous results for coordinates parallel to the surfaces collectively.

Table 1 Respective averaged squared amplitudes u^2 for Si and O atoms in the bilayer (x, y coordinates are parallel to the surface and z perpendicular)

		Si atoms	O atoms
Ru(0001)	$\langle u_x^2 \rangle$	2.55	2.62
	$\langle u_y^2 \rangle$	4.19	4.22
	$\langle u_z^2 \rangle$	0.0327	0.0402
1O	$\langle u_x^2 \rangle$	0.0481	0.0773
	$\langle u_y^2 \rangle$	0.0368	0.0665
	$\langle u_z^2 \rangle$	0.0237	0.0271
3O	$\langle u_x^2 \rangle$	0.371	0.440
	$\langle u_y^2 \rangle$	0.678	0.739
	$\langle u_z^2 \rangle$	0.0292	0.0374

affects the position of the entire bilayer film with respect to the metal underneath. These different stacking properties of the film depending on the different oxygen concentrations on the metal substrate has been observed in the experiments described below. These properties are the reason why different structures have to be combined in the LEED-I/V analysis.

4.3 Results and discussion of I/V-LEED experimental studies and its structural analysis

Based on the results of the calculation, presented above, we considered the shift of the bilayer silica film by superimposing a variety of structures. 47 different structural models have been developed following the scheme depicted in Fig. 8. A complete table of the used models is given in the ESI† with further details. A (2 × 2) unit cell was used in the dynamical-LEED calculations. For each high-symmetry model, the distance between the topmost Ru layer and the bottom layer of the bilayer film ($d_{Si–Ru}$) was varied from 2.2 Å up to 4.2 Å in steps of 0.2 Å. For each value $d_{Si–Ru}$, all the atoms in the bilayer SiO$_2$, the oxygen atoms at the interface layer and the Ru atoms down to the 2nd surface layer were allowed to fully relax respecting the symmetry constrains of each model. The Debye temperature of the Si (θ_D^{Si}) atoms, of the O (θ_D^{O}) atoms in the bilayer SiO$_2$ and in the interface layer (θ_D^{Oin}) and of the surface Ru atoms (θ_D^{Ru}) were fitted, while the Debye temperatures of the Ru bulk layers were kept fixed at θ_D^{Bulk} 415 K.[52]

In the high-symmetry models the centre of the bilayer SiO$_2$ hexagons lies on top of the high-symmetry substrate sites, namely fcc-hollow, hcp-hollow and top. For the fcc–hcp model the centre of the bilayer SiO$_2$ hexagons are halfway between the fcc and hcp hollow sites. These models have then been developed with different amounts of oxygen at the interface. The labels (1O), (2O) and (3O) stands for the number of oxygen atoms in the (2 × 2) unit cell at the interface.

In the mixed-O coverage models the coexistence of different number of oxygen atoms in (2 × 2) unit cell at the interface was investigated for each individual high-symmetry model. The label convention adopted here is as follows: (1O + 2O) means that, in this particular model, the coexistence of the 1O and 2O phases was allowed at the interface. The relative amount of each phase was varied from 0% to 100% keeping the total concentration equal to 100%. This was done as following:
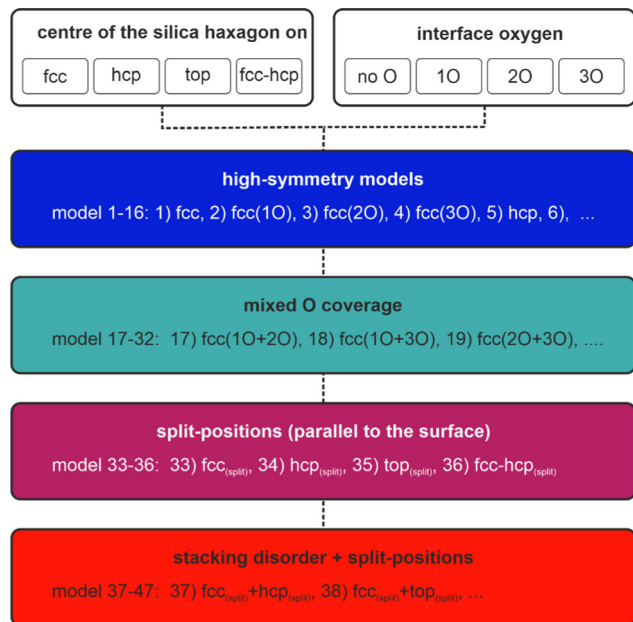
The amplitudes [u_z] for the bilayer on 1O and 3O show distinct behaviour. Although a similar transient period of equilibration appears within the first 20 ps, these amplitudes are somewhat smaller. They are within ±0.1 to ±0.15 Å. Bilayer motions of these systems in directions parallel to the surfaces are noticeably smaller than corresponding motions on the clean Ru(0001) surface. This can be readily explained by the PES cross sections discussed in the previous section. As the SiO$_3$ moieties are trapped by the substantial potential wells of *ca.* 4 eV depth, lateral mobility of the bilayer on the 1O surface structure is small. To quantify this mobility in a single number, we calculate average squared amplitudes following.[51] These numbers, which have been computed according to eqn (2) are summarized in Table 1. It is apparent that Si atoms and O atoms show similar oscillatory or mobility characteristics. Furthermore, each system features distinct motional behaviour parallel to the surface. Consistent with the minimal energy barriers for the clean Ru(0001) support, corresponding amplitudes are one order of magnitude larger than respective numbers for 3O. The 1O surface relates to the smallest amplitudes, being another order of magnitude smaller than those for the 3O system. Consequently, the lateral SiO$_2$ film motion or dynamics is largest on the Ru(0001) surface, it is one order of magnitude less pronounced for the 3O system and yet another order of magnitude smaller for the silica film on the 1O system. Therefore, the concentration of oxygen on the Ru(0001) surface

Fig. 8 Scheme for the developed trial models considered in the I/V-LEED analysis. A complete list with the achieved R_P factors is given in the ESI.†

Fig. 9 R_P factors for all the trial models considered in the LEED analysis. An additional table of this graph is provided in the ESI.†

$\sum_i x_i(\text{mixed-O})_i$, where x_i is the concentration of model (mixed-O)$_i$, i is equal to 2 or 3 (if two or three models are mixed, respectively), and $\sum_i x_i = 100\%$.

In the split-position model class (parallel to the surface), the split-position approach was introduced to simulate thermal vibrations with large amplitudes parallel to the surface for each high-symmetry models having the (3O) phase at the interface. The atoms were displaced from their equilibrium position by ±0.2 Å along the unit cell diagonals. The notation used here is: fcc$_{(split)}$ means that the split-position approach was introduced to the fcc$_{(3O)}$ model.

In the last class a stacking disorder plus split-position models have been introduced. Here the possibility of coexistence of different domains on the surface was investigated by mixing the high-symmetry models having the (3O) phase at the interface, after including large thermal vibrations through the split-position approach. The fraction of each domain on the surface was varied from 0% up to 100% always keeping the total concentration equal to 100%. This was done as following: $\sum_i x_i(\text{model})_i$, where x_i is the concentration of model (model)$_i$, i is equal to 2, 3 or 4 (if two, three or four different models are mixed, respectively), and $\sum_i x_i = 100\%$.

In all models where mixed domains were considered, the calculated spectra were derived from incoherently summing over the different terraces. In order to quantify the agreement between the experimental and theoretical I/V-LEED curves we have used the R-factor proposed by Pendry (R_P).[53]

In order to include vibrations with large amplitudes, the split-position approach was used in some models where the bilayer is allowed to vibrate with an amplitude of ±0.2 Å with
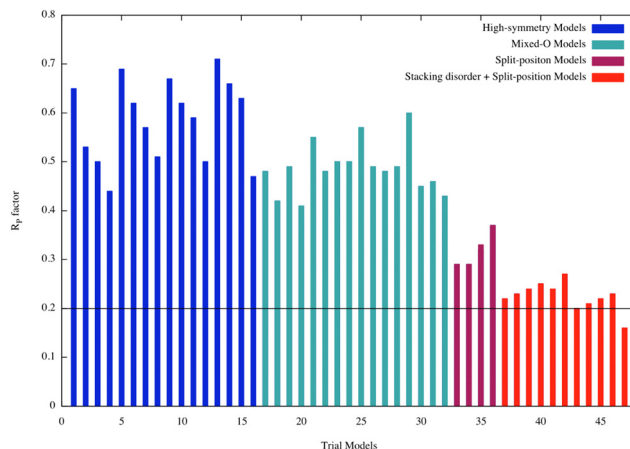
respect to the equilibrium position. The idea of split position is that the probability-density function describing the thermal vibrations can be approximated using a few distinct positions with an appropriate occupation factor.[54–56]

Fig. 9 shows the R_P factors obtained for all the structural models evaluated in this work. A detailed list can be found in Table S2 of the ESI.† The first set of models analyzed here were the high-symmetry ones (from 1 to 16). All of them exhibited R_P values higher than 0.44. For example, model 1–4, (01) fcc, (02) fcc(1O), (03) fcc(2O), (04) fcc(3O), R_P decreases from ~0.65 to ~0.44 due to the change in oxygen coverage. It is also important to observe that the R_P decreases when the oxygen coverage at the interface increases from 1 to 3 oxygen atoms in the (2×2) layer in the interface between the substrate and bilayer silica film (blue bars).

Since these first models did not properly describe the experimental I/V-LEED curves, a second class was considered where we allowed the coexistence of domains with different number of oxygen atoms at the interface (mixed-O models: from 17 to 32). Once more, a poor agreement between theory and experiment was obtained as shown in Fig. 9 (turquoise bars) indicating that new structural models must be considered.

According to our DFT calculations the bilayer silica film interacts with the Ru(0001) substrate through van der Waals forces and is weakly bound to the substrate. This weak interaction would allow the bilayer silica easily to vibrate parallel and perpendicularly to the surface. If these vibration models had large amplitudes and low frequencies, as we realized *via* the above-discussed calculations, they could have a strong influence in the scattering processes undergone by the incident electrons in the LEED experiment. Molecular dynamic simulations performed in this work, and presented in the previous section, demonstrated that the centre of mass of the bilayer silica vibrates with relatively large amplitude. Guided by the facts just explained, the next class of models considered in this LEED analysis was built by allowing the high-symmetry models to have large amplitude vibrations parallel to the surface (split-position models: from 33 to 36). The R_P factors obtained for this
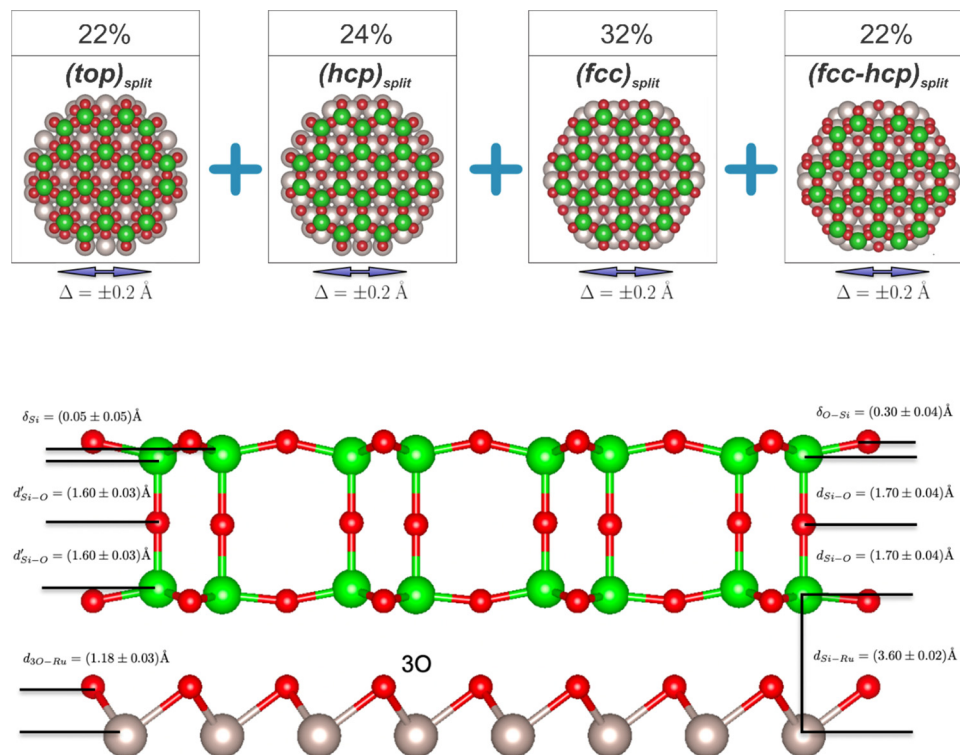
Fig. 10 (top panel) Schematic representation of the best model described by a R_P = 0.16. According to this model, the surface is covered by four different domains having the following concentrations: 22% of (top)$_{split}$, 24% of (hcp)$_{split}$, 32% of (fcc)$_{split}$, and 22% (fcc–hcp)$_{split}$. (lower panel) Side view of the best model showing the relevant structural parameters.

class of models are also presented in Fig. 9 (purple bars). An improvement in the agreement between the theoretical and experimental I/V-LEED curves is now observed as reflected by a decrease of the R_P factors.

As revealed by our theoretical calculations, different adsorption sites may have similar adsorption energies and the film may easily be shifted. Therefore, different structures may coexist on the surface. Real-space STM images of domain boundaries have also emphasized several possible registries of the bilayer with the underlying metal substrate.[57] To properly address this point, a new class of models was included in the LEED analysis (stacking disorder + split position models: from 37 to 47) and corresponding R_P factors are shown in Fig. 9 (red bars). The assumption of presence of stacking disorder greatly improved the agreement between theory and experiment and reduce the R_P factors from the range of 0.3 to 0.2. The lowest R_P factor value achieved of 0.16 corresponds to model 47 having 22% of (top)$_{split}$, 24% of (hcp)$_{split}$, 32% of (fcc)$_{split}$, and 22% (fcc–hcp)$_{split}$ domains covering the surface (Fig. 10 – top panel). A side view of the structure with the relevant structural parameters is presented in the lower panel of Fig. 9. The final structural parameters were calculated by averaging the corresponding structural parameters in the four different domains.

The uncertainty of Pendry R-factor is evaluated by calculating the $RR = \dfrac{varR}{R_{min}} = \sqrt{\dfrac{8V_{Oi}}{\Delta E}}$ where V_{oi} is the imaginary part of the inner potential and ΔE is total energy range defined by the experimental beams used in the structural determination.

In this study, the imaginary part of the inner potential was set to 7.5 eV (after optimization) and the total energy range is 2.610 eV resulting in a RR = 0.1516. The final $R_P = R_{min}(1 \pm RR) = (0.16 \pm 0.02)$. The final structural parameters and the respective error bars are presented in Fig. 10.

Fig. 11 shows the comparison between experimental (blue curves) and the theoretical (black curves) I/V-LEED curves corresponding to the best model is shown in Fig. 10. Most of the main features presented in the experimental curves are well reproduced in theory.

5. Summary and conclusions

Via a variety of surface science techniques in combination with theoretical electronic structure calculations, the structure of a silica bilayer on an oxygen covered Ru(0001) single crystal surface has been studied. It is shown that, since the bilayer is only bound by dispersive forces to the substrate, a detailed structure determination of all interatomic distances represents a challenge. Even though the STM data reveal a detailed structure of the top of the bilayer, the position of the entire bilayer with respect to the substrate is influenced by a number of parameters. In part, this became apparent when we tried to understand the kinetics of water formation at the interface between the bilayer and the substrate, used as model for a reaction in confined space. It was only possible to fit the observed apparent activation energy for the reaction, by assuming that the bilayer moves parallel and perpendicular to the
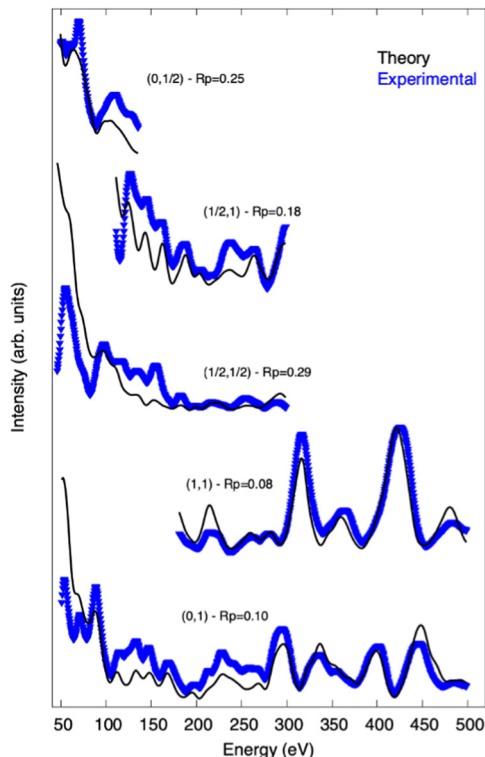
Fig. 11 Experimental (blue) and theoretical (black) I/V-LEED curves for the best model (R_P = 0.16) obtained from the LEED analysis. The (i, j) notation gives the index of the diffraction spots. The R_P for each individual beam is also shown. I/V-LEED curves of additional diffraction spots are given in the ESI.†

surface without influencing the internal silica bilayer film structure, as the amount of oxygen at the interface changes during the reaction. This observation triggered the idea to perform the present I/V-LEED study.

We find that for a given preparation of the silica film on the oxygen saturated Ru(0001) surface, a decent agreement between measured I/V-LEED data judged by the R_P factor, and theoretical modelling of the intensity *versus* voltage curves, can only be obtained, if a combination of structural components is considered. Also, this finding is consistent with the calculated soft phonon modes moving the film parallel to the surface, which are documented through the molecular-dynamics simulations. Also, and foremost, the bilayer silica film shows almost the same activation energies for a full oxygen coverage as compared with the clean Ru(0001) surface, while an intermediate coverage, documented *via* calculations for an oxygen coverage of one oxygen atom per unit cell leads to a much-reduced mobility. The overall results are fully consistent with the concepts of statistical stacking of the layers in layered materials, and also with observations made for supported graphene.

Data availability statement

Further theoretical and experimental results supporting this article have been uploaded as part of the ESI.† Additional data

supporting the findings is available from the authors upon request.

Conflicts of interest

There are no conflicts to declare.

Acknowledgements

References

1 F. J. Grunthaner and P. J. Grunthaner, *Mater. Sci. Rep.*, 1986, **1**, 65–160.
2 F. J. Himpsel, F. R. McFeely, A. Taleb-Ibrahimi, J. A. Yarmoff and G. Hollinger, *Phys. Rev. B: Condens. Matter Mater. Phys.*, 1988, **38**, 6084–6096.
3 H.-J. Freund, *Acc. Chem. Res.*, 2017, **50**, 446–449.
4 J.-Q. Zhong and H.-J. Freund, *Chem. Rev.*, 2022, **122**, 11172–11246.
5 X. Yu, B. Yang, J. Anibal Boscoboinik, S. Shaikhutdinov and H.-J. Freund, *Appl. Phys. Lett.*, 2012, **100**, 151608.
6 C. Zhou, X. Liang, G. S. Hutchings, J.-H. Jhang, Z. S. Fishman, R. Wu, A. Gozar, U. D. Schwarz, S. Ismail-Beigi and E. I. Altman, *Nanoscale*, 2019, **11**, 21340–21353.
7 X. Xu and D. W. Goodman, *Appl. Phys. Lett.*, 1992, **61**, 774–776.
8 X. Xu and D. W. Goodman, *Surf. Sci.*, 1993, **282**, 323–332.
9 K. Luo, D. Y. Kim and D. W. Goodman, *J. Mol. Catal. A: Chem.*, 2001, **167**, 191–198.
10 J. W. He, X. Xu, J. S. Corneille and D. W. Goodman, *Surf. Sci.*, 1992, **279**, 119–126.
11 T. Schroeder, M. Adelt, B. Richter, M. Naschitzki, M. Bäumer and H. J. Freund, *Surf. Rev. Lett.*, 2000, **07**, 7–14.
12 T. Schroeder, M. Adelt, B. Richter, M. Naschitzki, M. Bäumer and H. J. Freund, *Microelectron. Reliab.*, 2000, **40**, 841–844.
13 T. Schroeder, A. Hammoudeh, M. Pykavy, N. Magg, M. Adelt, M. Baumer and H. J. Freund, *Solid-State Electron.*, 2001, **45**, 1471–1478.
14 T. Schroeder, J. B. Giorgi, M. Bäumer and H. J. Freund, *Phys. Rev. B: Condens. Matter Mater. Phys.*, 2002, **66**, 165422.

15 D. Löffler, J. J. Uhlrich, M. Baron, B. Yang, X. Yu, L. Lichtenstein, L. Heinke, C. Büchner, M. Heyde, S. Shaikhutdinov, H. J. Freund, R. Włodarczyk, M. Sierka and J. Sauer, *Phys. Rev. Lett.*, 2010, **105**, 146104.

16 J. Weissenrieder, S. Kaya, J. L. Lu, H. J. Gao, S. Shaikhutdinov, H. J. Freund, M. Sierka, T. K. Todorova and J. Sauer, *Phys. Rev. Lett.*, 2005, **95**, 076103.

17 B. Yang, W. E. Kaden, X. Yu, J. A. Boscoboinik, Y. Martynova, L. Lichtenstein, M. Heyde, M. Sterrer, R. Włodarczyk, M. Sierka, J. Sauer, S. Shaikhutdinov and H.-J. Freund, *Phys. Chem. Chem. Phys.*, 2012, **14**, 11344–11351.

18 R. Włodarczyk, M. Sierka, J. Sauer, D. Löffler, J. J. Uhlrich, X. Yu, B. Yang, I. M. N. Groot, S. Shaikhutdinov and H. J. Freund, *Phys. Rev. B: Condens. Matter Mater. Phys.*, 2012, **85**, 085403.

19 L. Lichtenstein, C. Büchner, B. Yang, S. Shaikhutdinov, M. Heyde, M. Sierka, R. Włodarczyk, J. Sauer and H.-J. Freund, *Angew. Chem., Int. Ed.*, 2012, **51**, 404–407.

20 L. Lichtenstein, M. Heyde and H.-J. Freund, *Phys. Rev. Lett.*, 2012, **109**, 106101.

21 M. J. Prieto, T. Mullan, M. Schlutow, D. M. Gottlob, L. C. Tănase, D. Menzel, J. Sauer, D. Usvyat, T. Schmidt and H.-J. Freund, *J. Am. Chem. Soc.*, 2021, **143**, 8780–8790.

22 M. J. Prieto, H. W. Klemm, F. Xiong, D. M. Gottlob, D. Menzel, T. Schmidt and H.-J. Freund, *Angew. Chem., Int. Ed.*, 2018, **57**, 8749–8753.

23 L. Lichtenstein, M. Heyde and H.-J. Freund, *J. Phys. Chem. C*, 2012, **116**, 20426–20432.

24 N. Marom, J. Bernstein, J. Garel, A. Tkatchenko, E. Joselevich, L. Kronik and O. Hod, *Phys. Rev. Lett.*, 2010, **105**, 046801.

25 M. Položij, H. V. Thang, M. Rubeš, P. Eliášová, J. Čejka and P. Nachtigall, *Dalton Trans.*, 2014, **43**, 10443–10450.

26 Y. Zhang, M. Položij and T. Heine, *Chem. Mater.*, 2022, **34**, 2376–2381.

27 W. Zhao, S. M. Kozlov, O. Höfert, K. Gotterbarm, M. P. A. Lorenz, F. Viñes, C. Papp, A. Görling and H.-P. Steinrück, *J. Phys. Chem. Lett.*, 2011, **2**, 759–764.

28 G. Kresse and J. Furthmüller, *Phys. Rev. B: Condens. Matter Mater. Phys.*, 1996, **54**, 11169–11186.

29 G. Kresse and J. Furthmüller, *Comput. Mater. Sci.*, 1996, **6**, 15–50.

30 P. E. Blöchl, *Phys. Rev. B: Condens. Matter Mater. Phys.*, 1994, **50**, 17953–17979.

31 G. Kresse and D. Joubert, *Phys. Rev. B: Condens. Matter Mater. Phys.*, 1999, **59**, 1758–1775.

32 J. P. Perdew, K. Burke and M. Ernzerhof, *Phys. Rev. Lett.*, 1996, **77**, 3865–3868.

33 H. J. Monkhorst and J. D. Pack, *Phys. Rev. B: Solid State*, 1976, **13**, 5188–5192.

34 S. Grimme, *J. Comput. Chem.*, 2006, **27**, 1787–1799.

35 T. Kerber, M. Sierka and J. Sauer, *J. Comput. Chem.*, 2008, **29**, 2088–2097.

36 F. R. Rehak, G. Piccini, M. Alessio and J. Sauer, *Phys. Chem. Chem. Phys.*, 2020, **22**, 7577–7585.

37 L. Gura, S. Tosoni, A. L. Lewandowski, P. Marschalik, Z. Yang, W.-D. Schneider, M. Heyde, G. Pacchioni and H.-J. Freund, *Phys. Rev. Mater.*, 2021, **5**, L071001.

38 S. Tosoni and J. Sauer, *Phys. Chem. Chem. Phys.*, 2010, **12**, 14330–14340.

39 R. Jinnouchi, K. Miwa, F. Karsai, G. Kresse and R. Asahi, *J. Phys. Chem. Lett.*, 2020, **11**, 6946–6955.

40 R. Jinnouchi, F. Karsai and G. Kresse, *Phys. Rev. B*, 2020, **101**, 060201.

41 S. Nosé, *J. Chem. Phys.*, 1984, **81**, 511–519.

42 W. G. Hoover, *Phys. Rev. A: At., Mol., Opt. Phys.*, 1985, **31**, 1695–1697.

43 R. Jinnouchi, F. Karsai and G. Kresse, *Phys. Rev. B*, 2019, **100**, 014105.

44 N. Nilius, A. Corper, G. Bozdech, N. Ernst and H. J. Freund, *Prog. Surf. Sci.*, 2001, **67**, 99–121.

45 L. Lichtenstein, C. Büchner, B. Yang, S. Shaikhutdinov, M. Heyde, M. Sierka, R. Włodarczyk, J. Sauer and H.-J. Freund, *Angew. Chem., Int. Ed.*, 2012, **51**, 404–407.

46 H. W. Klemm, M. J. Prieto, F. Xiong, G. B. Hassine, M. Heyde, D. Menzel, M. Sierka, T. Schmidt and H.-J. Freund, *Angew. Chem., Int. Ed.*, 2020, **59**, 10587–10593.

47 K. M. Burson, H. J. Yang, D. S. Wall, T. Marsh, Z. Yang, D. Kuhness, M. Brinker, L. Gura, M. Heyde, W.-D. Schneider and H.-J. Freund, *J. Phys. Chem. C*, 2022, **126**, 3736–3742.

48 A. L. Lewandowski, P. Schlexer, C. Büchner, E. M. Davis, H. Burrall, K. M. Burson, W.-D. Schneider, M. Heyde, G. Pacchioni and H.-J. Freund, *Phys. Rev. B*, 2018, **97**, 115406.

49 A. Mayer, H. Salopaasi, K. Pussi and R. D. Diehl, *Comput. Phys. Commun.*, 2012, **183**, 1443–1447.

50 A. Barbieri and M. A. Van Hove, *SATLEED and Phase Shift package*, 1994, **https://www.icts.hkbu.edu.hk/vanhove/Van Hove_files/leed/leedpack.html**.

51 M. Baudin and K. Hermansson, *Surf. Sci.*, 2001, **474**, 107–113.

52 C. Y. Ho, R. W. Powell and P. E. Liley, *J. Phys. Chem. Ref. Data*, 1972, **1**, 279–421.

53 J. B. Pendry, *J. Phys. C: Solid State Phys.*, 1980, **13**, 937–944.

54 T. Hertel, H. Over, H. Bludau, M. Gierer and G. Ertl, *Phys. Rev. B: Condens. Matter Mater. Phys.*, 1994, **50**, 8126–8129.

55 H. Over, W. Moritz and G. Ertl, *Phys. Rev. Lett.*, 1993, **70**, 315–318.

56 C. Stampfl, M. Scheffler, H. Over, J. Burchhardt, M. Nielsen, D. L. Adams and W. Moritz, *Phys. Rev. B: Condens. Matter Mater. Phys.*, 1994, **49**, 4959–4972.

57 K. M. Burson, C. Büchner, M. Heyde and H. J. Freund, *J. Phys.: Condens. Matter*, 2017, **29**, 035002.